



Effect of Heat Input on the Microstructural, Mechanical, and Corrosion Properties of Dissimilar Weldment of Conventional Austenitic Stainless Steel and Low-Nickel Stainless Steel

Vipin Tandon¹ · Manish A. Thombre² · Awanikumar P. Patil² · Ravindra V. Taiwade² · Himanshu Vashishtha³

Received: 20 March 2020 / Revised: 5 September 2020 / Accepted: 9 September 2020 / Published online: 25 September 2020
© The Author(s) 2020

Abstract

In the present investigation, an attempt has been made to investigate the replacement compatibility of conventional austenitic stainless steel (316L) with low-Ni austenitic stainless steel (201) by employing their dissimilar welding using gas tungsten arc welding technique with varying heat input. The effects of heat input on the microstructural, mechanical, and corrosion properties were studied. The result depicts the balanced austenite/ferrite content in the fusion zone for both the heat inputs. The low heat input process, which results in a faster cooling rate, demonstrates higher tensile strength and microhardness. Similarly, the pitting corrosion resistance of the fusion zone demonstrates better properties on the low heat input process attributed to the lesser dendritic length and lesser interdendritic arm spacing.

Keywords Low-nickel austenitic stainless steels · Dissimilar welding · Mechanical properties · Electrochemical behavior

Introduction

Austenitic stainless steels (SSs) are extensively consumed material in industries owing to their good mechanical and corrosion properties [1, 2]. In conventional austenitic SSs, nickel (Ni) is the major alloying element to stabilize the austenite phase at room temperature and therefore is termed as

chrome-nickel (Cr-Ni) austenitic SSs, i.e., 300 series. However, an increase in the Ni price is driving industries to use low-Ni or Ni-free austenitic SSs, in which Ni is substituted by other austenite stabilizing elements, such as nitrogen (N) and manganese (Mn) [3]. This leads to the development of Cr-Mn-Ni-N austenitic SSs, i.e., 200 series [3], with the same Cr content (18%). The low-nickel austenitic stainless steels are more prominent because of their great combination of strength, ductility, and corrosion resistance properties with better cost-effectiveness. In 201 austenitic SS, the 5–7 wt.% Mn is added to stabilize the austenite phase and the addition of Ni is minimized from 9 to 11% to 3–5%, thus making the material cost-effective [3, 4]. Moreover, the addition of N in the austenitic SS enhances the mechanical and corrosion properties of the austenitic SSs [5, 6]. Therefore, 201 austenitic SS possesses a great potential to replace the widely used conventional 316L-type Cr-Ni austenitic SSs due to their good agreement of mechanical and corrosion properties [7].

In industries, fusion welding is a mostly used technique to join the austenitic SSs. Fusion welding of dissimilar metals or alloys is always challenging due to differences in composition, physical, and thermal properties as it is associated with many defects such as solidification cracking, porosities, and micro-segregation [8]. Among these defects, solidification cracking majorly affects the properties of the weldment. In austenitic

✉ Vipin Tandon
vipintandon3103@gmail.com

✉ Himanshu Vashishtha
vashishtha.himanshu100593@gmail.com

Manish A. Thombre
manish17thombre@gmail.com

Awanikumar P. Patil
appatil14@gmail.com

Ravindra V. Taiwade
rvtaiwadevnt@gmail.com

¹ Centre of Sustainable Built Environment, Manipal School of Architecture and Planning, Manipal Academy of Higher Education, Manipal 576104, India

² Department of Metallurgical and Materials Engineering, Visvesvaraya National Institute of Technology, Nagpur 440010, India

³ Department of Materials Science and Engineering, Indian Institute of Technology, New Delhi, Delhi 110016, India

SSs weldment, the presence of ferrite plays a very important role in solidification cracking and controlling its volumetric fraction can prevent such defects [9]. Hence, the WRC-1992 is mostly employed in the majority of the literature to predict the volumetric fraction of ferrite [9, 10]. Therefore, it becomes very important to identify the welding process parameters which will result in an optimum volumetric fraction of ferrite and thus gives the best mechanical and corrosion properties and can have a longer life. The micro-segregation is also a major problem in the fusion welding of two different metals as it can deteriorate the weld quality. Many studies have been conducted on the effects of welding processes and parameters on the micrographs and mechanical properties of similar welding of conventional 316L austenitic SS. Moslemi et al. [11] examined the effect of current on the gas metal arc-welded 316L austenitic SS. They concluded that high current input weld possesses superior mechanical properties. Durgutlu [12] investigated the effect of hydrogen mixing in argon as shielding gas in tungsten inert gas arc-welded 316L austenitic SS. The author concluded that 1.5% H₂ in argon improved the mechanical properties of 316L weldments. Samanta et al. [13] investigated the effect of welding speed on the laser-welded 316L austenitic SS. They reported that ferrite content in the weld zone and the oxidation rate of the weldment decreased on increasing the welding speed. Verma et al. [14] performed the dissimilar welding of 316L austenitic SS with 2205 duplex SS with varying heat input. They reported that high heat input weldment depicted better mechanical and corrosion properties than low heat input weldment. Prabakaran et al. [15] conducted the laser welding process of 316L austenitic SS with 1080 low carbon steel and optimized the laser welding process for the better mechanical properties.

In a view of the similarity between costly conventional Cr-Ni austenitic SSs and cheaper Cr-Mn-Ni-N austenitic SS in terms of mechanical and corrosion properties, the substitution of 316L austenitic SS by 201 austenitic SS up to some degree of replacement in service failures of equipment can be a viable option. Moreover, low-nickel grades have been employed in power plant condensers for few applications [16]. In this regard, Vashishtha et al. [9] have studied the dissimilar welding of 304/201 austenitic stainless steels using different welding processes and filler electrodes. Also, the industries are concerned to use the high-performance materials for an aggressive environment and the use of cheaper materials for mild environment, which indicates the use of dissimilar welds. In this context, to lower the use of costly 316L austenitic SS,

the dissimilar welding of 316L austenitic SS with marginally cheaper 304L austenitic SS has been studied by some researchers [17, 18]. However, the industrial question arises that if a 316L austenitic SS fails during their service, is it possible to substitute it with cheaper 201 austenitic SS? Hence, the main objective of this paper is to understand the replacement of conventional 316L austenitic SS up to some degree in service failures of equipment with cheaper 201 austenitic SS. If a fusion welding is performed to join the 201 austenitic SS with 316L austenitic SS, it becomes important to investigate the effect of welding processes and its parameters on mechanical and corrosion properties.

Therefore, the present study investigates the effect of heat input on the dissimilar welding of 316L austenitic SS with 201 austenitic SS using a 316L austenitic SS filler electrode by gas tungsten arc welding (GTAW) technique.

Materials and Methods

The base materials (316L and 201 austenitic SS) used in the present study were procured in the form of hot-rolled sheets (3 ± 0.05 mm), and their chemical compositions obtained by optical emission spectroscopy are given in Table 1. The samples (80 mm × 80 mm × 3 mm) were cut using a wire-cut electrical discharge machine (EDM) and solution annealed at 1050°C for 1 h, followed by water quenching. The dissimilar weld joints of 316L-201 austenitic SS were prepared by the GTAW welding process using a 316L austenitic SS filler electrode with varying heat input. The heat input (Q) was calculated by Eq. (1) having 60% efficiency for the GTAW process [9, 19]:

$$Q = \eta VI/v \quad (1)$$

where V is arc voltage in volts, I is welding current in amperes and v is welding speed in mm/s.

The welding process details are reported in Table 2.

For microstructural examination, the transverse section of the welded samples was cut by a wire-cut EDM machine. The samples were then abraded on series of emery papers followed by cloth polishing smeared with alumina powder, cleaned ultrasonically in distilled water for 5 min, and etched in 10 g oxalic acid at 1 Acm⁻² for 90 s galvanostatically, as per the ASTM A-262, practice A test [20]. The metallographic examination was then performed in Zeiss Axio Lab A1 optical

Table 1 Chemical composition of BMs and filler electrode

Materials	C	Ni	Mo	Cr	Mn	P	Si	S	N	Fe
316L ASS	0.018	10.62	2.15	16.85	1.32	0.02	0.29	0.01	...	Bal.
201 ASS	0.09	4.12	...	17.39	5.24	0.03	0.26	0.01	0.15	Bal.
E/ER 316L ASS	0.016	11.12	2.11	17.41	1.57	0.02	0.27	0.01	...	Bal.

Table 2 Welding parameters used in GTAW process

	Current (A)	Voltage (V)	Welding speed (mm/s)	Heat input (KJ/mm)
HHI	90	11.4	1.4	0.7328
LHI	110	12.6	2.5	0.5544

microscopy and scanning electron microscopy (SEM JEOL 6380) coupled with energy-dispersive spectroscopy (EDS) to estimate the chemical composition of various phases. The microhardness test was carried out across the length of the samples using Vickers microhardness tester at 300 g load applied for 10 s, as per the ASTM E92 standard [21]. The δ -ferrite content was estimated by ferritoscope (Fisher SMP-30). For the tensile test of welded specimens, samples of 120 mm length, 12 mm width, and 54 mm gauge length are cut using wire-cut EDM machine. The tensile test of the welded specimens was carried out by a universal testing machine (Instron 4667) with a crosshead speed of 0.5 mm min^{-1} , as per the ASTM E8 standard [22]. The fractography analysis of the fractured specimens was then examined using SEM to understand the nature of the fracture.

The electrochemical analysis, i.e., electrochemical impedance spectroscopy (EIS) and potentiodynamic polarization (PDP), was performed in potentiostat (Biologic VMP-300) using standard three-electrode cell setup. The cell consisted of a working electrode (test specimen), reference electrode (saturated calomel electrode) and counter electrode (platinum gauze), performed in 3.5% NaCl media. The open-circuit potential (OCP) was measured for 1 h, during which the potential stabilized followed by EIS and PDP tests. The EIS was measured in the frequency range of 10^6 to 10^{-2} Hz with a ± 10 mV sinusoidal AC signal. The PDP tests were performed in the potential range of $-0.5 V_{\text{OCP}}$ to $+0.7 V_{\text{OCP}}$ at a scan rate of 0.167 mV/sec. The obtained data were then analyzed using EC-Lab software.

Results and Discussion

Microstructural Analysis of Welded Samples

Solidification Mode and Estimation of δ -ferrite Content

The chemical composition of base metal and filler electrode determines the solidification mode in the FZ according to Eqs. (2) and (3) [23]:

$$\text{Cr}_{\text{eq}} = \text{Cr} + \text{Mo} + 0.7\text{Nb} \quad (2)$$

$$\text{Ni}_{\text{eq}} = \text{Ni} + 35\text{C} + 20\text{N} + 0.25\text{Cu} \quad (3)$$

The solidification mode in austenitic SSs can be determined by $\text{Cr}_{\text{eq}}/\text{Ni}_{\text{eq}}$ using WRC-1992 diagram and is divided into four following equations [24]:

$$\text{Austenite(A)mode} : L \rightarrow (L + \gamma) \rightarrow \gamma; \text{Cr}_{\text{eq}}/\text{Ni}_{\text{eq}} < 1.25 \quad (4)$$

$$\begin{aligned} &\text{Austenite – Ferrite(AF)mode} : \\ &L \rightarrow (L + \gamma) \rightarrow (L + \gamma + \delta) \rightarrow (\gamma + \delta); \\ &1.25 < \text{Cr}_{\text{eq}}/\text{Ni}_{\text{eq}} < 1.48 \end{aligned} \quad (5)$$

$$\begin{aligned} &\text{Ferrite – Austenite(FA)mode} : \\ &L \rightarrow (L + \delta) \rightarrow (L + \delta + \gamma) \rightarrow (\gamma + \delta); \\ &1.48 < \text{Cr}_{\text{eq}}/\text{Ni}_{\text{eq}} < 1.95 \end{aligned} \quad (6)$$

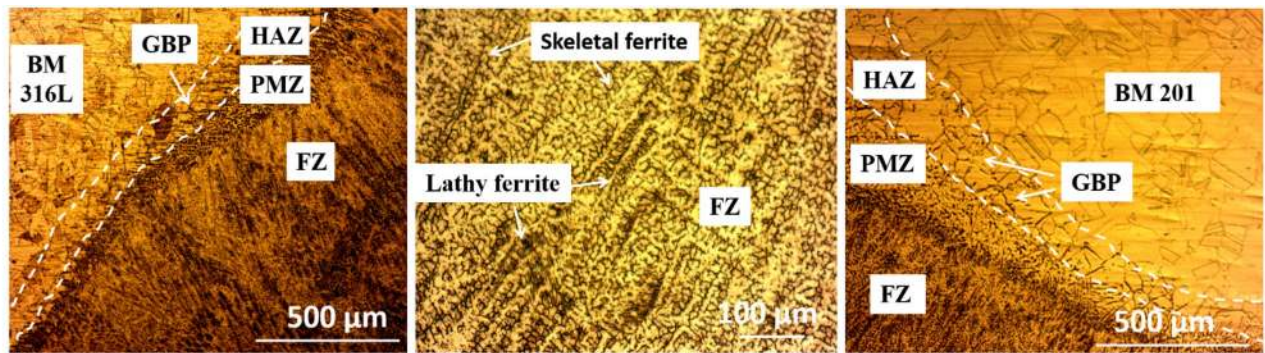
$$\text{Ferrite(F)mode} : L \rightarrow (L + \delta) \rightarrow \delta \rightarrow (\gamma + \delta); \text{Cr}_{\text{eq}}/\text{Ni}_{\text{eq}} > 1.95 \quad (7)$$

In the present study, the calculated value of $\text{Cr}_{\text{eq}}/\text{Ni}_{\text{eq}}$ is 1.68, and therefore, the solidification mode is found out to be FA mode (as per Eq. 6). The δ -ferrite content in the FZ in terms of ferrite number (average of ten readings is taken) measured by ferritoscope for LHI- and HHI-welded samples is estimated to be 9.05 and 6.87 units, respectively. It can be noticed that δ -ferrite content in the FZ decreased with increasing heat input. The cooling rate is relatively higher in the LHI process which results in a steep thermal gradient of the weld metal and lesser time for the transformation of δ -ferrite to γ phase. As the mode of solidification is FA and upon cooling, the primary δ -ferrite solidifies in FZ and transforms to $\delta \rightarrow \gamma$. The transformation of $\delta \rightarrow \gamma$ is a diffusion-controlled process, and slower cooling rate in HHI process offers sufficient time to transform δ -ferrite to γ phase. Therefore, a more γ phase is formed in FZ at the HHI process.

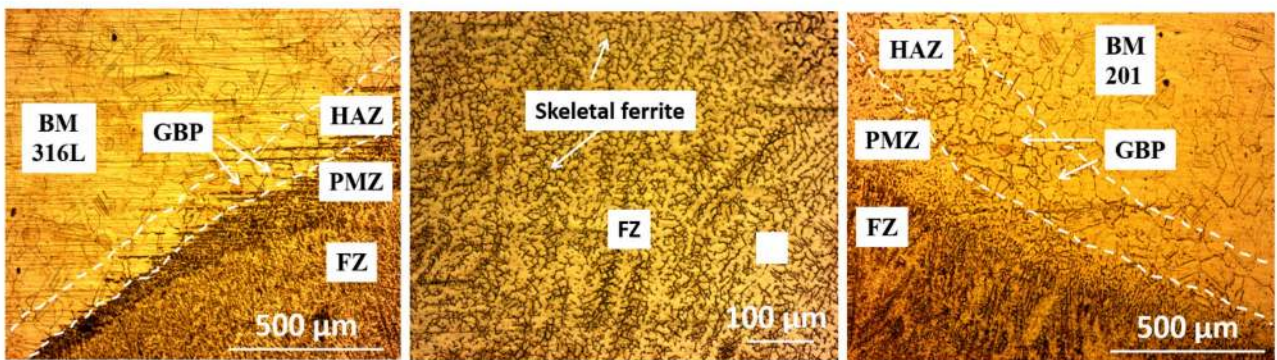
Microstructural Evolution

The optical micrographs of welded samples are shown in Fig. 1a–b. In both the welded samples, the microstructural evolution can be categorized into various zones, namely (i) fusion zone (FZ), (ii) partially melted zone (PMZ), (iii) heat-affected zone (HAZ), and (iv) unaffected zone, i.e., base metal (BM) on both sides of weldments.

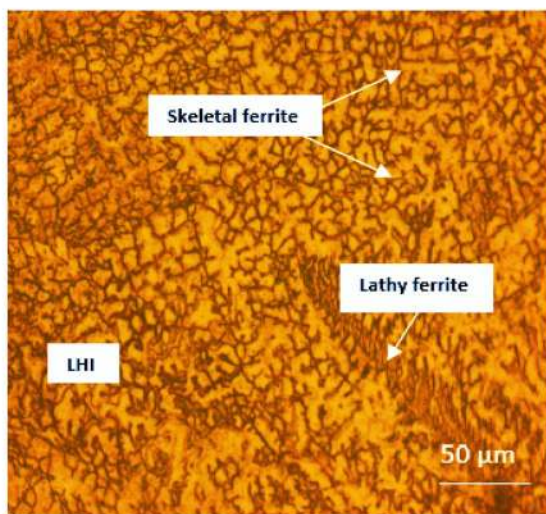
The FZ of both the weld joints contains δ -ferrite (dark phase) with an interdendritic layer of austenite (light phase) as shown in Fig. 1c–d. The columnar growth of FZ was observed for both the heat input processes. The amount of δ -ferrite in the FZ can be inferred from the thermal cycle experienced during welding [9]. In FZ, LHI weldment depicts the formation of δ -ferrite in the form of skeletal and lathy morphology. However, the FZ of HHI weldment



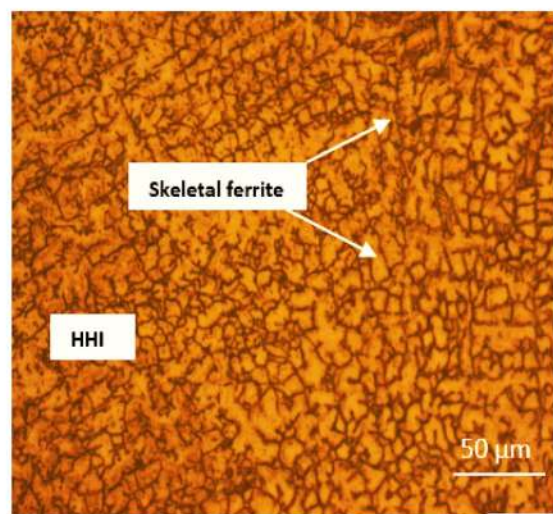
(a)



(b)



(c)



(d)

Fig. 1 The microstructural evolution in dissimilar welded 316L-201 austenitic SS by (a) LHI and (b) HHI process and magnified optical micrographs of FZ for (c) LHI and (d) HHI process

depicts the formation of δ -ferrite in the form of skeletal morphology only. The LHI process possesses a faster cooling rate and subsequently more amount of δ -ferrite retained in

the FZ; furthermore, the skeletal morphology of δ -ferrite transformed into lathy morphology. This can be attributed to constrained diffusion during $\delta \rightarrow \gamma$ transformation.

Table 3 Microstructural details of weld metals

Samples	Dendrite length (μm)	Interdendritic arm spacing (μm)
FZ LHI	71.07	40.78
FZ HHI	98.42	52.63

Moreover, Table 3 shows the measured values (ten readings were measured, and the average is calculated) of dendritic length and interdendritic arm spacing of both the processes. It can be observed that the dendritic length and interdendritic arm spacing increase with increase in heat input. The faster cooling rate in the LHI process might help in suppressing the dendritic size and cell spacing formation as reported by authors [25, 26]. Therefore, the increase in dendritic length and interdendritic arm spacing in the HHI process can be ascribed to a slower cooling rate.

In both the weldments, the zone next to FZ is termed as PMZ. In PMZ, the BM has been melted and re-solidified. The zone next to PMZ is HAZ. The HAZ was significantly affected by the heat input during welding. It was noticed that the HAZ width increased with an increase in heat input for both the sides of the weldments. This can be ascribed to a slower cooling rate possessed by the HHI weldment. On the other hand, the width of HAZ for the 201 austenitic SS side is higher than the 316L austenitic SS side. This can be ascribed to the higher susceptibility of 201 austenitic SS toward intergranular precipitation [27].

Mechanical Properties of Welded Samples

Microhardness Measurement

The microhardness measurements across the various zones, namely FZ, PMZ, HAZ, and BM, were measured, and the results are shown in Fig. 2. It can be observed that the microhardness value of HAZ is lower as compared to FZ for both the weldments. This can be due to carbon segregation [9]. Significant grain coarsening of the HAZ results in lower microhardness compared to FZ. The HAZ of 201 austenitic SS side was much affected than the 316L austenitic SS side due to the segregation of carbon at a much faster rate [9]. Also, it can be noticed that the microhardness value of LHI FZ is higher as compared to HHI FZ. This is due to a faster cooling rate, which resulted in a fine structure with less interdendritic spacing [25, 26]. In PMZ of both the 316L austenitic SS and 201 austenitic SS side, high microhardness values can be observed in both LHI and HHI processes. This can be due to the presence of partly un-melted grains at the fusion boundary, which acts as a prominent nucleation site for the new precipitating phase during the solidification

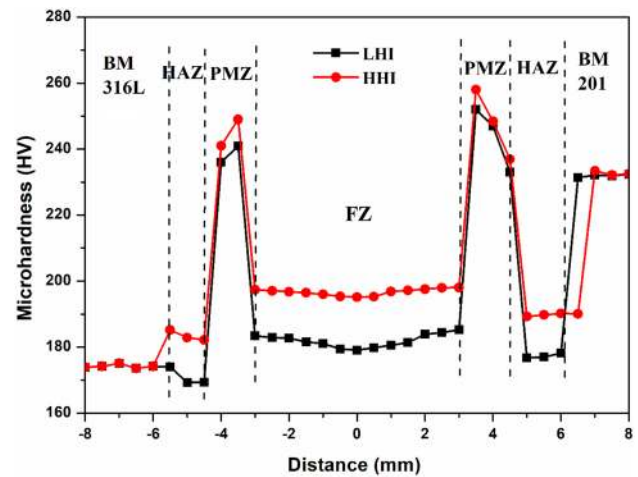


Fig. 2 Microhardness profile of dissimilar welded 316L-201 austenitic SS

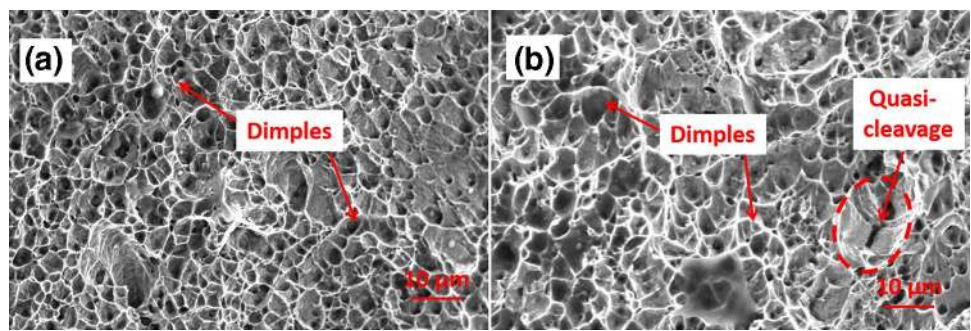
stage [25, 28]. It should be noted that, in HAZ, the area close to PMZ shows lower microhardness values attributed to the coarse-grained structure, while the area close to BM shows higher microhardness values attributed to the fine-grained structure. This can be attributed to the slow cooling rate experienced by the area adjacent to the PMZ [29].

Tensile Measurement

The ultimate tensile strength (UTS) of LHI and HHI weldments was measured as 582 and 567 MPa, respectively. This higher UTS for LHI weldment can be attributed to a faster cooling rate, which resulted in higher δ -ferrite content and finer ferrite morphology with less interdendritic spacing [25, 26].

For both the weldments, the fracture occurred at HAZ on the 201 austenitic SS side. As can be in microhardness results, the microhardness values of HAZ are lower as compared to FZ and BM due to carbon segregation, thus making the HAZ relatively softer region. As can be seen from the optical results (Fig. 1), the width of HAZ and carbide precipitation is more in 201 austenitic SS side for both the weldments, and therefore, the fracture took place in the HAZ of 201 austenitic SS side. The fractography of the fractured samples was analyzed using SEM, and the results are shown in Fig. 3. It can be observed that on both the weldments, the fractography results show the uniform dimples which indicate the mode of fracture to be ductile in nature. Moreover, a small amount of quasi-cleavage feature can also be seen in the HHI weldment.

Fig. 3 SEM fractography images of (a) LHI and (b) HHI process



Electrochemical Behavior of Welded Samples

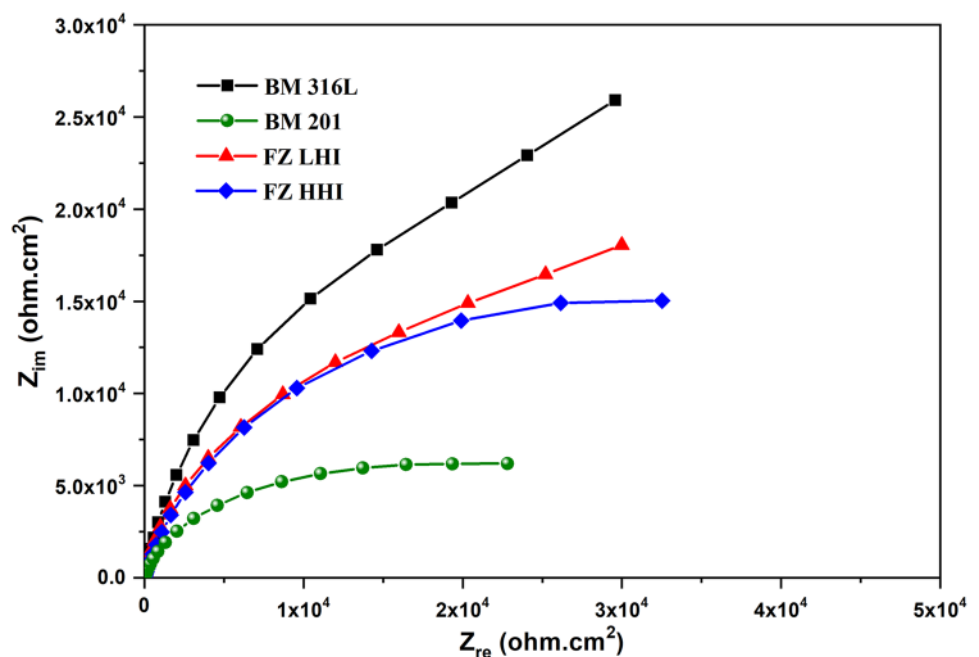
Electrochemical Impedance Spectroscopy Test

The EIS tests were performed to evaluate the resistance of passive film of FZ and BM of weldments in 3.5% NaCl. The EIS Nyquist plots of FZs and BMs of weldments are shown in Fig. 4. It can be observed that all the plots show unfinished semicircular arc with varying diameter. The diameter of the plots indicates the resistance of the film; more the diameter of the plots, more will the resistance of the passive film and consequently more corrosion resistance [30]. It can be observed from Fig. 4 that the diameter of Nyquist plot of 316L austenitic SS BM is more, while the diameter of Nyquist plot of 201 austenitic SS BM is the least. This can be attributed to the higher alloying elements (Mo and Ni) in 316L austenitic SS BM, and FZs are more compared to 201 austenitic SS [31]. Figure 5 represents the estimated chemical composition of δ -ferrite and γ phase in FZ of the

weldment estimated by EDS analysis. It can be observed from Fig. 5 that δ -ferrite phase contains more Cr and Mo and less Ni content than the γ phase. Moreover, the LHI FZ shows a higher diameter of the Nyquist plot as compared to that of HHI FZ.

Furthermore, the EIS Bode plots of the FZs and BMs are shown in Fig. 6. In Bode plots, the impedance modulus at low-frequency region signifies the resistance to corrosion, while the higher impedance values at high-frequency region signify the passive film compactness [31, 32]. Similar to the Nyquist plots, the higher impedance values can be seen for 316L BM, while the least can be observed for 201 austenitic SS BM. In the same way, the impedance value for LHI FZ is more as compared to HHI FZ. A similar trend can be seen for impedance modulus at low-frequency region. Hence, these results indicate that LHI FZ depicts more corrosion resistance than HHI FZ. This can be attributed to fine-grained structure in the LHI FZ [26].

Fig. 4 EIS Nyquist plots of BMs and FZs



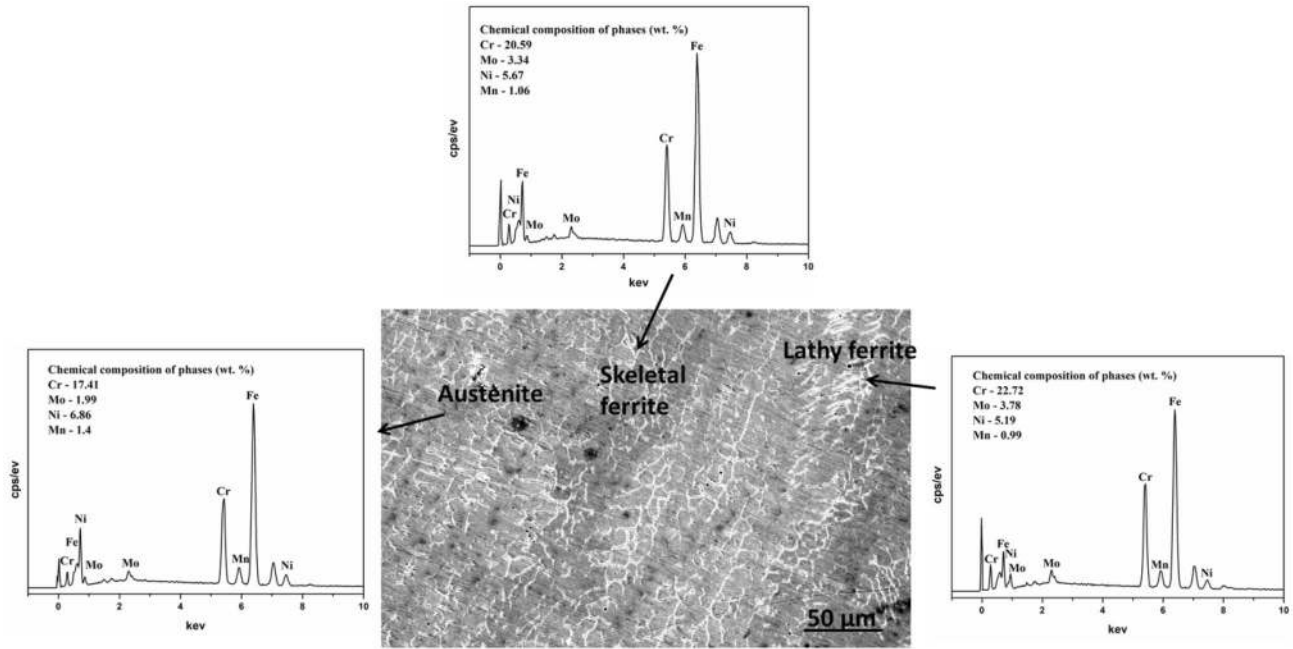
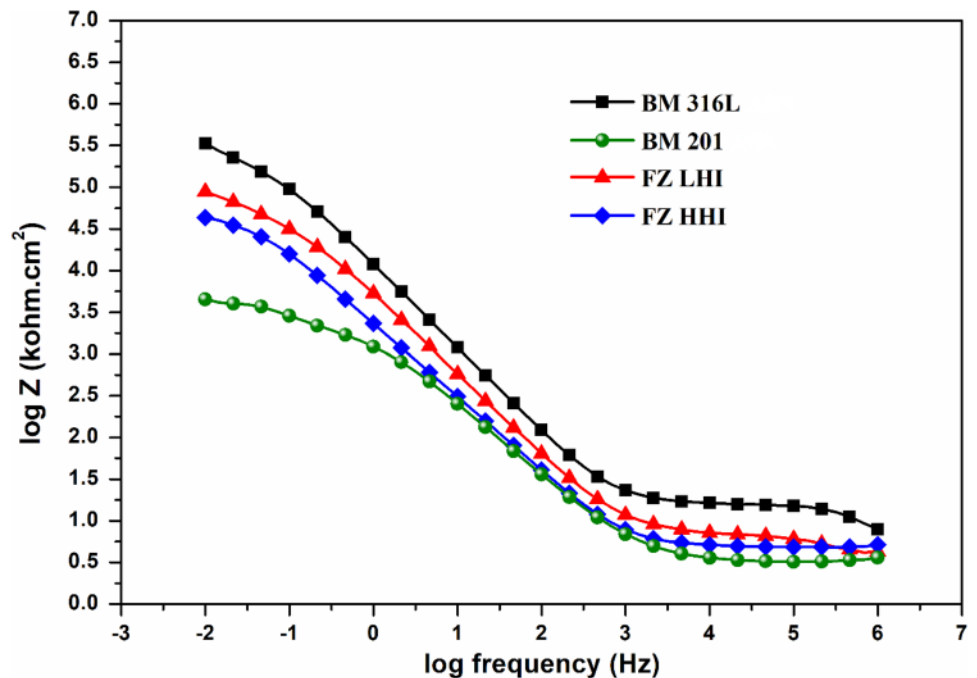


Fig. 5 EDS analysis and its chemical composition of various phases in FZ

Fig. 6 EIS Bode plots of BMs and FZs



Potentiodynamic Polarization Test

The PDP test is performed to evaluate the corrosion rate of FZ and BM of weldments in 3.5% NaCl in terms of corrosion current density (i_{corr}). The PDP plots are shown in Fig. 7. The anodic part of the plots is divided into three regions, namely (i) active region, (ii) passive region, and

(iii) trans-passive region. In the active region, the current density increased rapidly followed by the passive region where current density increased slowly. In the trans-passive region, after a certain potential value, the current density increased drastically and the potential is taken as pitting potential (E_{pit}). The electrochemical parameters such as i_{corr} and corrosion potential (E_{corr}) are estimated

Fig. 7 PDP plots of BMs and FZs

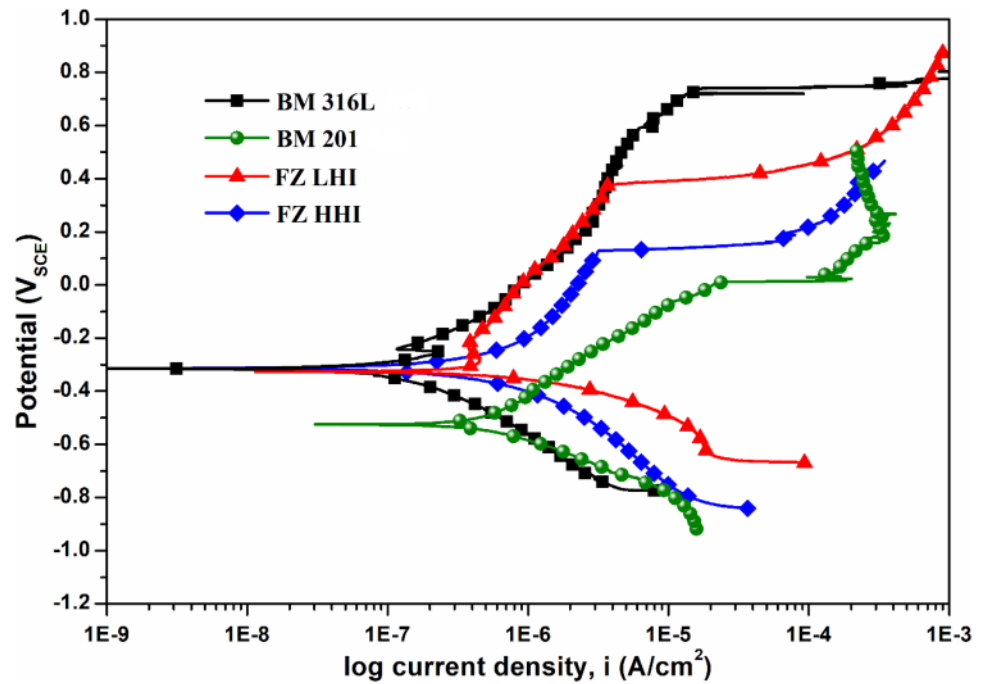


Table 4 Electrochemical parameters obtained from PDP plots of FZs and BMs

Samples	E_{corr} (V_{SCE})	i_{corr} ($\mu\text{A}/\text{cm}^2$)	E_{pit} (V_{SCE})
FZ LHI	-324.79	1.36	0.32
FZ HHI	-320.65	1.89	-0.07
BM 316L ASS	-314.65	0.34	0.73
BM 201 ASS	-525.21	8.41	0.01

from these plots using Tafel extrapolation and are given in Table 4.

It can be observed from Table 4 that i_{corr} value is least for the 316L austenitic SS BM, while the i_{corr} value is highest for 201 austenitic SS BM. This indicates 316L austenitic SS exhibits better corrosion resistance than 201 austenitic SS. In other words, 201 austenitic SS is more prone to corrosion than 316L austenitic SS, as corrosion rate is directly proportional to i_{corr} value. Also, the E_{pit} value of 316L austenitic SS is more than the 201 austenitic SS. It has been reported that higher the E_{pit} values, higher is the corrosion resistance. Hence, the better corrosion resistance of 316L austenitic SS can be attributed to the higher alloying elements (Mo and Ni) as more compared to 201 austenitic SS [31]. Interestingly, it can be noticed from Table 4 that the E_{pit} values for LHI FZ and HHI FZ are higher than the 201 austenitic SS BM. This shows that the LHI FZ and HHI FZ depict better corrosion resistance than the 201 austenitic SS BM. This can be attributed to the 316L austenitic SS filler electrode which contains higher alloying elements than the 201 austenitic SS BM. However, it can also be noticed from Table 4 that the E_{pit}

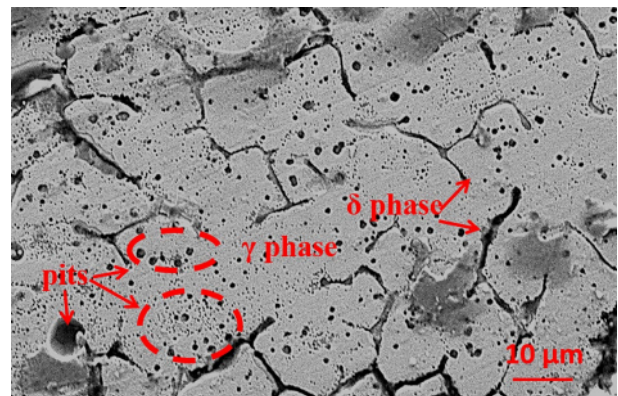


Fig. 8 SEM micrograph of FZ of pitted sample after PDP test

values of LHI FZ are higher than the HHI FZ. Furthermore, the LHI FZ depicts lower i_{corr} value as compared to that of HHI FZ. The better corrosion resistance of LHI FZ can be attributed to the smaller dendritic length and interdendritic arm spacing as shown in Table 3. Figure 8 shows the SEM micrograph of pits formed in FZ after the PDP test. It can be observed that most of the pits are formed in the γ phase, their grain boundary, and the interface region of γ -austenite and δ -ferrite, while very fewer pits can be seen in δ -ferrite phase. Hence, it can be stated that the microstructure existence and their grain size play a very significant part in defining the corrosion behavior of the welded specimen. Chuai-phan and Srijaroenpramong [25] stated that smaller dendrites and lesser interdendritic spacing in FZ produced by the LHI

(faster cooling rate) exhibit better corrosion resistance than FZ having larger dendrites and more interdendritic spacing produced by the HHI (slower cooling rate). Therefore, the LHI weldment exhibits better corrosion resistance than HHI weldment. These results are consistent with the results obtained by EIS Nyquist and Bode plots and also are consistent with the findings of other authors [25, 26].

Conclusions

The dissimilar welding of 316L austenitic SS and 201 austenitic SS was successfully welded using the GTAW process with varying heat inputs without any weld defects. The following conclusions can be drawn:

- (i) The skeletal and lathy ferrite was formed in a fusion zone of the low heat input weldment. The increase in heat input reduced the formation of lathy ferrite, and only, skeletal ferrite was formed in high heat input fusion zone.
- (ii) The high heat input process resulted in the more width of heat-affected zone for both the sides of base metals, attributed to the slower cooling rate. Moreover, the width of heat-affected zone is more for 201 austenitic SS base metal in both the heat input processes.
- (iii) The grain coarsening was observed in the heat-affected zone of both sides, and the extent of grain coarsening increased with an increase in heat input.
- (iv) The lesser dendritic length and lesser interdendritic spacing were found in the low heat input process, and therefore, the higher tensile strength was obtained for low heat input process.
- (v) The pitting corrosion resistance of the fusion zone of low heat input process demonstrates better resistance as compared to the high heat input process in 3.5% NaCl. This can be attributed to the smaller dendrite length and lesser inter-dendrite spacing in the fusion zone.

Funding Open access funding provided by Manipal Academy of Higher Education, Manipal.

Open Access This article is licensed under a Creative Commons Attribution 4.0 International License, which permits use, sharing, adaptation, distribution and reproduction in any medium or format, as long as you give appropriate credit to the original author(s) and the source, provide a link to the Creative Commons licence, and indicate if changes were made. The images or other third party material in this article are included in the article's Creative Commons licence, unless indicated otherwise in a credit line to the material. If material is not included in the article's Creative Commons licence and your intended use is not permitted by statutory regulation or exceeds the permitted use, you will

need to obtain permission directly from the copyright holder. To view a copy of this licence, visit <http://creativecommons.org/licenses/by/4.0/>.

References

1. M. Amitava, P.K. De, D.K. Bhattacharya, P.K. Srivastava, D.C. Jiles, Ferromagnetic properties of deformation-induced martensite transformation in AISI 304 stainless steel. *Metall. Mater. Trans. A* **35**, 599–605 (2004)
2. J.P. Schille, Z. Guo, N. Saunders, A.P. Miodownik, Modeling phase transformations and material properties critical to processing simulation of steels. *Mater. Manuf. Process.* **26**, 137–143 (2011)
3. R. Dalipi, L. Borgese, A. Casaroli, M. Boniardi, U. Fittschen, K. Tsuji, L.E. Depero, Study of metal release from stainless steels in simulated food contact by means of total reflection X-ray fluorescence. *J. Food Eng.* **173**, 85–91 (2016)
4. N. Nakada, N. Hirakawa, T. Tsuchiyama, S. Takaki, Grain refinement of nickel-free high nitrogen austenitic stainless steel by reversion of eutectoid structure. *Scr. Mater.* **57**, 153–156 (2007)
5. T. Masumura, N. Nakada, T. Tsuchiyama, S. Takaki, T. Koyano, K. Adachi, The difference in thermal and mechanical stabilities of austenite between carbon- and nitrogen-added metastable austenitic stainless steels. *Acta Mater.* **84**, 330–338 (2015)
6. Y. Fu, X. Wu, E.N. Han, W. Ke, K. Yang, Z. Jiang, Effects of nitrogen on the passivation of nickel-free high nitrogen and manganese stainless steels in acidic chloride solutions. *Electrochim. Acta* **54**, 4005–4014 (2009)
7. S.S.M. Tavares, J.M. Pardal, M.J.G.D. Silva, H.F.G. Abreu, M.R.D. Silva, Deformation induced martensitic transformation in a 201 modified austenitic stainless steel. *Mater. Charact.* **60**, 907–911 (2009)
8. N. Arivazhagan, S. Singh, S. Prakash, G.M. Reddy, Investigation on AISI 304 austenitic stainless steel to AISI 4140 low alloy steel dissimilar joints by gas tungsten arc, electron beam and friction welding. *Mater. Des.* **32**, 3036–3050 (2011)
9. H. Vashishtha, R.V. Taiwade, S. Sharma, A.P. Patil, Effect of welding processes on microstructural and mechanical properties of dissimilar weldments between conventional austenitic and high nitrogen austenitic stainless steels. *J. Manuf. Processes.* **25**, 49–59 (2017)
10. C.C. Silva, H.C. Miranda, H.B.D. Santana, J.P. Farias, Austenitic and ferritic stainless steel dissimilar weld metal evaluation for the applications as-coating in the petroleum processing equipment. *Mater. Des.* **47**, 1–8 (2013)
11. N. Moslemi, N. Redzuan, N. Ahmad, T.N. Hor, Effect of current on characteristic for 316 stainless steel welded joint including microstructure and mechanical properties. *Procedia CRIP.* **26**, 560–564 (2015)
12. A. Durgutlu, Experimental investigation of the effect of hydrogen in argon as a shielding gas on TIG welding of austenitic stainless steel. *Mater. Des.* **25**, 19–23 (2004)
13. S.K. Samanta, S.K. Mitra, T.K. Pal, Influence of welding speed on microstructure and oxidation behaviour of laser welded austenitic stainless steels. *ISIJ Int.* **46**, 100–105 (2006)
14. J. Verma, R.V. Taiwade, Dissimilar welding behavior of 22% Cr series stainless steel with 316L and its corrosion resistance in modified aggressive environment. *J. Manuf. Processes.* **24**, 1–10 (2016)
15. M.P. Prabakaran, G.R. Kannan, Optimization of laser welding process parameters in dissimilar joint of stainless steel AISI316/

- AISI1018 low carbon steel to attain the maximum level of mechanical properties through PWHT. *Opt. Laser Technol.* **112**, 314–322 (2019)
16. D.N. Wasnik, A failure study of condenser tube manufactured from low nickel stainless steels. *Eng. Fail. Anal.* **23**, 69–75 (2012)
 17. H.M. Soltani, M. Tayebi, Comparative study of AISI 304L to AISI 316L stainless steels joints by TIG and Nd:YAG laser welding. *J. Alloy. Compd.* **767**, 112–121 (2018)
 18. N. Kumar, M. Mukherjee, A. Bandyopadhyay, Comparative study of pulsed Nd:YAG laser Welding of AISI 304 and AISI 316 stainless steels. *Opt. Laser Technol.* **88**, 24–39 (2017)
 19. W.C. Jiang, B.Y. Wang, J.M. Gong, S.T. Tu, Finite element analysis of the effect of welding heat input and layer number on residual stress in repair welds for a stainless steel clad plate. *Mater. Des.* **32**, 2851–2857 (2011)
 20. H. Shaikh, N. Sivaibharasi, B. Sai, T. Anita, R. Amirthalingam, B.P.C. Rao, T. Jayakumar, H.S. Khatak, B. Raj, Use of eddy current testing method in detection and evaluation of sensitisation and intergranular corrosion in austenitic stainless steels. *Corros. Sci.* **48**, 1462–1482 (2006)
 21. Standard Test Method for Vickers hardness of metallic materials, E92-82, ASTM, PA, USA, 2003
 22. T.H. Lee, H.Y. Ha, J.Y. Kang, B. Hawang, W. Woo, E. Shin, In situ and ex situ neutron diffraction study on deformation behavior of high-nitrogen, Ni-free duplex stainless steel. *Scr. Mater.* **67**, 141–144 (2012)
 23. D.J. Kotecki, T.A. Sievert, WRC-1992 constitution diagram for stainless steel weldmetals: a modification of the WRC-1988 diagram. *Weld. J.* **71**, 171s–178s (1992)
 24. K. Rajasekhar, C.S. Harendranath, R. Raman, S.D. Kulkarni, Microstructural evolution during solidification of austenitic stainless steel weld metals: a color metallographic and electron microprobe analysis study. *Mater. Charact.* **38**, 53–65 (1997)
 25. W. Chuaiphana, L. Srijaoenpramong, Effect of welding speed on microstructures, mechanical properties and corrosion behavior of GTA-welded AISI 201 stainless steel sheets. *J. Mater. Process Technol.* **214**, 402–408 (2014)
 26. A.V. Bansod, A.P. Patil, S. Shukla, Effect of heat on microstructural, mechanical and electrochemical evaluation of tungsten inert gas welding of low-nickel ASS. *Anti-Corr. Met. Mater.* **65**, 605–615 (2018)
 27. M. Coetzee, P.G.H. Pistorious, The welding of experimental low-nickel Cr-Mn-N stainless steels containing copper. *J. S. Afr. Inst. Min. Met.* **96**, 99–108 (1995)
 28. H. Naffakh, M. Shamanian, F. Ashrafizadeh, Dissimilar welding of AISI 301 austenitic stainless steel to nickel-based alloy Inconel 657. *J. Mater. Process. Technol.* **209**, 3628–3639 (2009)
 29. F. Karci, R. Kacar, S. Gündüz, The effect of process parameter on the properties of spot welded cold deformed AISI 304 grade austenitic stainless steel. *J. Mater. Process. Technol.* **209**, 4011–4019 (2009)
 30. V. Tandon, A.P. Patil, R.C. Rathod, S. Shukla, Influence of cold work on electrochemical behavior of 316L ASS in PEMFC environment. *Mater. Res. Exp.* **5**, 026528 (2018)
 31. V. Tandon, A.P. Patil, R.C. Rathod, Enhanced corrosion resistance of Cr-Mn ASS by low temperature salt bath nitriding technique for the replacement of convectional Cr-Ni ASS. *Anti-Corr. Met. Mater.* **66**, 439–445 (2019)
 32. K.-C. Chang, M.-H. Hsu, H.-I. Lu, M.-C. Lai, P.-J. Liu, C.-H. Hsu, W.-F. Ji, T.-L. Chuang, Y. Wei, J.-M. Yeh, W.-R. Liu, Room-temperature cured hydrophobic epoxy/graphene composites as corrosion inhibitor for cold-rolled steel. *Carbon* **66**, 144–153 (2014)

Publisher's Note Springer Nature remains neutral with regard to jurisdictional claims in published maps and institutional affiliations.